



OPEN

## Sulfated endospermic nanocellulose crystals prevent the transmission of SARS-CoV-2 and HIV-1

Enrique Javier Carvajal-Barriga<sup>1,2,5</sup>, Wendy Fitzgerald<sup>3,5</sup>, Emiliós K. Dimitriadis<sup>4</sup>, Leonid Margolis<sup>3</sup> & R. Douglas Fields<sup>1</sup>✉

Biomaterials with antimicrobial activity are gaining attention due to their biodegradability and efficacy in interacting with a wide range of microorganisms. A new cellulose nano-biomaterial, endospermic nanocellulose crystals (ENC) obtained from parenchymal tissue of ivory nut endosperm, has a natural capacity as a universal binder. This feature is enhanced when it is chemically functionalized, and can be exploited in the fight against microbes. We tested the ability of sulfated ENC in aqueous suspension to encapsulate viruses through a crosslinking reaction mediated by cations. 0.25% w/v ENC suspensions efficiently encapsulated spike (S) protein, preventing its interaction with ACE2 receptor. ENC was further able to encapsulate SARS-CoV-2 pseudoviruses and prevent infection of 293T-hsACE2 cells. ENC also suppressed infection of MT-4 cells with HIV-1<sub>LAI.04</sub>. This antiviral activity of sulfated ENC is due to the irreversible interaction of ENC with viral particles mediated by crosslinking, as antiviral activity was less effective in the absence of cations. Additionally, ENC was used as a matrix to immobilize recombinant ACE2 receptors and anti-S IgG, creating molecular lures that efficiently inhibited SARS-CoV-2 infections in vitro. These results show that sulfated ENC from ivory nuts can be used as an efficient antiviral material.

The primary mode of SARS-CoV-2 transmission is inhalation of respiratory droplets, thus the use of masks is recommended to limit transmission. Numerous epidemiologic studies have shown that masking reduced transmission<sup>1</sup>. Air filtration by HEPA filters also reduced virus in the air by 65–90%<sup>2</sup>. One method to further reduce viral transmission would be to develop materials that combine filtration with antimicrobial properties.

Towards this goal we proposed the use of cellulose nanoparticles to encapsulate viral particles thus preventing their passage. These nanocellulose particles were designed with dense sulfate charges obtained from ivory nuts from a palm tree from the *Arecaceae* family that grows in tropical regions of South America. Due to its derivation from the endosperm of the palm's seed, it was designated endospermic nanocellulose (ENC). The unique primary cell walls yielded more homogeneous and thinner cellulose nanoparticles compared to cell walls from other vegetal tissues. The thinner the nanoparticles, the higher the surface area of the suspended material to interact with the viruses. This material could be used as a film for masks and filters to bind viral particles, increasing the effectiveness of these filtration devices.

Here, we demonstrated two different methods of blocking transmission of virus using sulfonated ENC. One was non-specific that consisted of the direct binding (nanoencapsulation) of the SARS-CoV-2 pseudovirus particles, or encapsulation of 293T-hsACE2 target cells. ENC also efficiently encapsulated HIV-1 virions and prevented transmission to MT-4 target cells. The second method was highly specific using molecular lures, anti-SARS-CoV-2 spike (S) protein antibodies and soluble ACE2 receptors, immobilized in nanocellulose scaffolding to specifically bind viral particles.

<sup>1</sup>Nervous System Development and Plasticity Section, Eunice Kennedy Shriver National Institute of Child Health and Human Development, National Institutes of Health, Bethesda, MD, USA. <sup>2</sup>Neotropical Center for the Biomass Research, Pontificia Universidad Católica del Ecuador, Quito, Pichincha, Ecuador. <sup>3</sup>Section On Intercellular Interactions, Eunice Kennedy Shriver National Institute of Child Health and Human Development, National Institutes of Health, Bethesda, MD, USA. <sup>4</sup>Biomedical Engineering and Physical Science Shared Resource Program, National Institute of Biomedical Imaging and Bioengineering, National Institutes of Health, Bethesda, MD, USA. <sup>5</sup>These authors contributed equally: Enrique Javier Carvajal Barriga and Wendy Fitzgerald. ✉email: fieldsd@mail.nih.gov

Antiviral activity of specific biomaterials depends on different modes of action such as the interference with virus entry in cells; the destruction of viral structures; the inhibition of replication of nucleic acids; and the inhibition of virus release from infected cells<sup>3,4</sup>. Sodium alginate, a soluble salt of alginic acid that crosslinks in presence of Ca<sup>++</sup> ions, has been tested with successful results against several viruses, including SARS-CoV-2 and HIV-1. The antiviral mechanisms include anionic interaction of alginic acid with viral surface proteins that interferes with viral receptor binding, inhibition of capsid synthesis, and the aggregation and encapsulation of viral particles which limits their infectivity<sup>5</sup>. Recently, sialic acid has also been found to bind to a specific domain in the S protein of SARS-CoV-2, which can be exploited to inhibit SARS-CoV-2 infection<sup>6</sup>. Although sialic acid is not a nanoparticle itself, it can be assembled into scaffolds with the capability to encase viruses.

Nanocellulose is a universal binder due to its high surface area that creates intricate networks supported by oriented attachments that facilitate multiple interactions between the nanoparticles themselves, and with other similar sized particles, with high interfacial energy and Brownian motion<sup>7</sup>. Nanocelluloses are utilized in coatings, energy storage devices, binders of natural fibers and composites, wound dressings, bone and cartilage restoration, drug delivery systems, tissue engineering, and an ever-increasing number of biotechnology and biomedical applications<sup>8</sup>. Recent studies have shown the feasibility of developing nanocellulose-based antimicrobial materials<sup>9,10</sup>. Nanocelluloses can interact with a wide range of biological entities including eukaryotic cells, bacteria, and viruses, and the type of interaction can be engineered through chemical synthesis<sup>11,12</sup>.

Cellulose nanoparticles result from the deconstruction of larger cellulose microfibrils. Both nanocellulose synthesis strategies and the source of cellulose fibers affect the type and the properties of the resulting material<sup>13</sup>. Aqueous suspensions of nanocellulose form hydrogels whose stabilization is a consequence of electrostatic and steric repulsions<sup>14</sup>. Functionalized nanocellulose with half-ester sulfate groups hold negative charges that create repulsion among the suspended nanoparticles, resulting in stable, single-phase colloid suspensions with time-independent rheological properties<sup>14,15</sup>. The supramolecular interactions between sulfated nanocellulose particles and other particles within the nanoscopic scale (including viruses) rely on the formation of linkages or electrostatic interactions between cellulose's active groups and charged moieties in proteins such as those on the surface of microbes.

Nanoparticles are prone to combat SARS-CoV-2 through agglutination around viral particles, and these antiviral properties can be programmed based on varying functional requirements. A recent report on nanocellulose, as a delivery system for the antiviral agent curcumin, was effective against SARS-CoV-2<sup>16</sup>. Nevertheless, no previous investigation focused on the use of nanocellulose particles to bind viruses or to entrap cell receptors or anti SARS-CoV-2 specific antibodies to create molecular lures.

In this research, we utilized the gelification property of sulfated nanocellulose to nanoencapsulate viruses, namely SARS-CoV-2 and HIV-1, and to immobilize molecular lures specific for SARS-CoV-2, to inhibit viral transmission. The nanoencapsulation is due to anionic interactions between sulfate groups in modified cellulose particles and positive charges in the virus membrane and surrounding medium. This prevents the viruses from binding to their cell receptors, namely ACE2 for SARS-CoV-2<sup>17</sup> and CD4 and coreceptor (CCR5 or CXCR4) for HIV-1<sup>18</sup>.

## Results

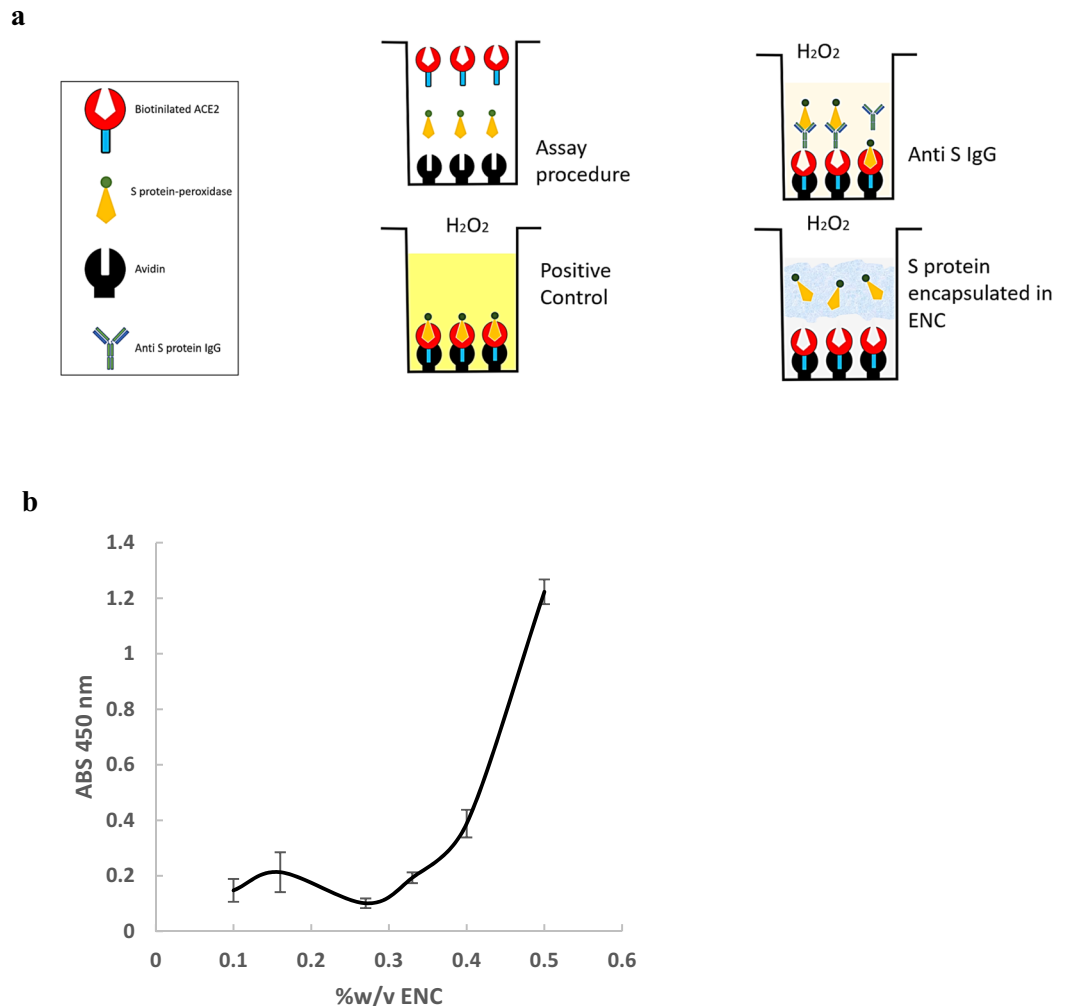
**ENC encapsulation of S protein prevented binding to ACE2 in ELISA tests.** To determine whether ENC can encapsulate SARS-CoV-2 S protein thus preventing interaction with ACE2, and to establish an optimal working concentration of ENC, we used the quantitative SARS-CoV-2 neutralizing antibody ELISA with modifications. Spike protein labeled with horse radish peroxidase (HRP) was preincubated with ENC suspension prior to its addition in ELISA wells then combined with biotinylated ACE2 receptor, which attaches to avidin coated plate wells. HRP-labeled S protein that binds ACE2 within the well was then measured after addition of HRP substrate. HRP enzymatic activity was directly proportional to the amount of S protein that escapes ENC. A diagram of the assay is depicted in Fig. 1a.

When S protein was preincubated in 0.27% w/v ENC before addition to the assay, the absorbance units (AU) obtained were below the limit of detection ( $0.142 \pm 0.008$  AU compared to lowest standard measurement of  $0.291 \pm 0.053$  AU,  $n = 3$ ). This indicated that S protein was irreversibly bound by ENC and was not able to react with ACE2. Validity of the assay was confirmed by use of two positive controls containing anti-SARS-CoV-2 S IgG provided with the kit and each gave measurements in the expected range provided with the assay instructions.

To determine the optimal ENC concentration for nanoencapsulating S protein, one experiment was run using a series of dilutions of ENC (0.5, 0.4, 0.33, 0.27, 0.16, and 0.1)% w/v with the addition of 0.9% w/v NaCl solution. The lower the absorbance, the more effective the S protein nanoencapsulation. According to the absorbance curve, we determined that 0.27% w/v ENC suspension was the optimal concentration ( $n = 3$ , Fig. 1b).

**AFM and fluorescence confocal microscopy demonstrated encapsulation of S protein in ENC.** To demonstrate at the nanoscopic scale the interactions and crosslinking of ENC particles around the S protein clumps we used atomic force microscopy (AFM). This technique revealed intricate networks of ENC that were denser (bright spots) when attached to S protein clumps (Fig. 2a). This is due to a higher affinity of ENC to protein clumps than to other ENC particles caused by anionic interactions between the cellulose nanoparticles and protein positive moieties.

Confocal microscopy was employed to demonstrate at the micro scale the agglutination of S protein in ENC matrix, and to verify the identity of the presumed S protein clumps seen by AFM. The protein interaction with ENC was evident even after a series of washing cycles, suggesting the nanoencapsulation of protein clumps is irreversible. To demonstrate that, hydrogels encapsulating Alexa Fluor 488 (AF488) labeled S protein were crosslinked, washed in triplicate, and dried followed by confocal microscopy analysis. Figure 2b shows the same



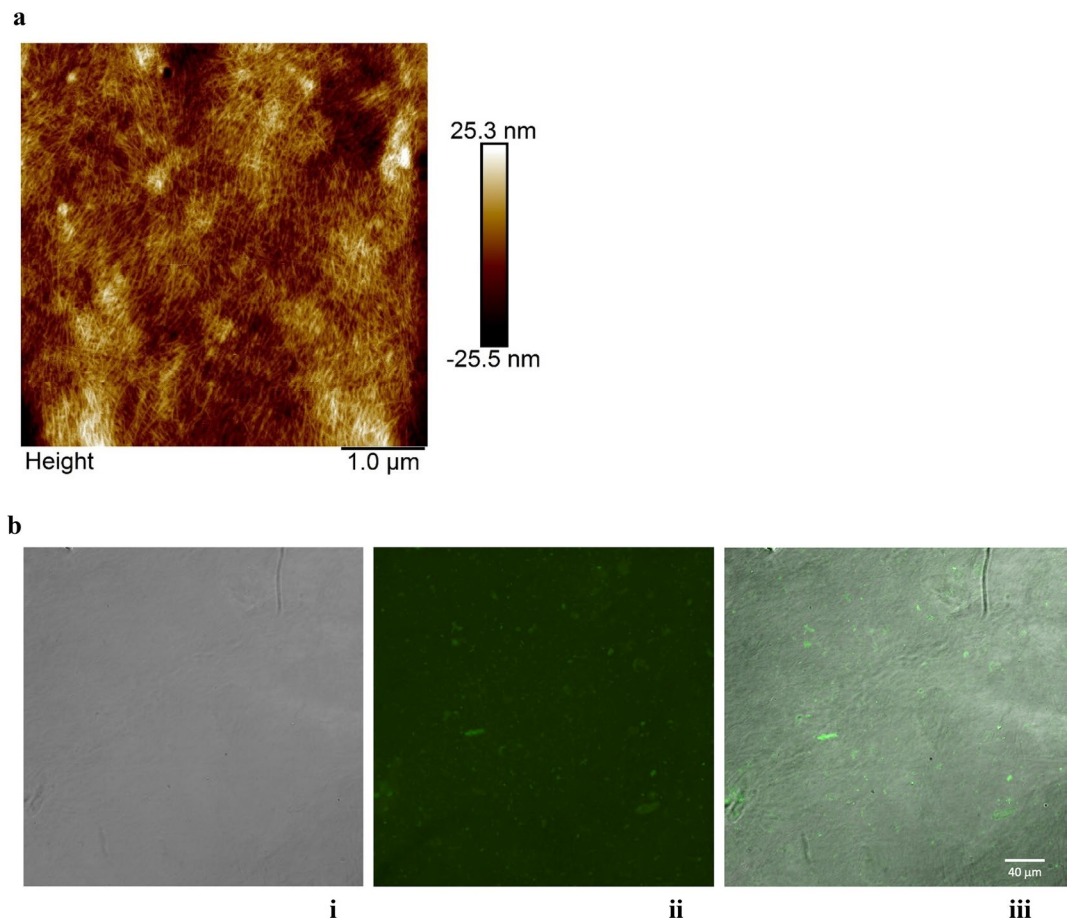
**Figure 1.** ELISA experiments of S-protein encapsulation vs anti S IgG docking. A modified ELISA protocol was used to demonstrate that SARS-CoV-2 S protein can be entrapped in endospermic nanocellulose (ENC) thus preventing its binding to ACE2. (a) Schematic of the modified ELISA protocol for encapsulation of S protein. The assay was modified to measure the ability of ENC to block the interaction of S protein with ACE2, rather than the ability of anti-S neutralizing antibody to block this interaction; (b) The modified ELISA was used to determine optimum % of ENC suspension (expressed in w/v) to efficiently encapsulate S protein; lower absorbance equals higher S protein encapsulation ( $n = 3$ ).

image with different filters: (i) confocal differential interference contrast image of the ENC membrane, (ii) AF488 confocal images of fluorescent clumps of S protein and (iii) overlay of DIC and AF488 images showing the fluorescent clumps of S protein on the ENC membrane.

**SARS-CoV-2 S pseudovirus cell entry was inhibited by ENC.** To test whether ENC can prevent virus transmission, 293T-hsACE2 cells were inoculated with SARS-CoV-2 pseudovirus (pv) with a green fluorescent protein (GFP) reporter in conditions with and without ENC and analyzed by flow cytometry three days later.

SARS-CoV-2 pv entrapped in ENC or captured by recombinant ACE2 protein (ACE2) or anti-SARS-CoV-2 S IgG (IgG) entrapped in ENC was not able to infect cells:  $0.003 \pm 0.003\%$ ,  $0.007 \pm 0.004\%$ , and  $0.022 \pm 0.010\%$  of infected cells respectively ( $p < 0.0001$ ), ( $n = 16$ , Fig. 3a and dot plots in Suppl. Fig. 1). Meanwhile, for controls in which SARS-CoV-2 pv was added without ENC, the number of cells infected was  $1.76 \pm 0.08\%$  ( $n = 16$ ). Preincubation of SARS-CoV-2 pv with either ACE2 or IgG did not significantly change virus transmission ( $1.94 \pm 0.19\%$  and  $1.28 \pm 0.10\%$  infected cells, respectively, Fig. 3a). The low level of infection with SARS-CoV-2 pv entrapped by ENC or captured by ACE2 or IgG in ENC was not different than background in uninfected controls ( $n = 9$ ,  $p = 0.388-0.993$ ). These results were confirmed by fluorescent microscopy as well, where a similar pattern of GFP+ cells was observed (Suppl. Fig. 2a-f).

We next evaluated whether cells could be protected from infection by entrapping the cells in ENC. Cells were first embedded in ENC and then inoculated with SARS-CoV-2 pv in culture medium or SARS-CoV-2 pv in ENC. SARS-CoV-2 pv infection was evaluated by fluorescent microscopy. Cells were cultured as above then the gels were transferred to microscope slides at day 3 post-inoculation, stained with propidium iodide, cover-slipped and



**Figure 2.** AFM and fluorescence images showed encapsulation of S protein Atomic force microscopy image of encapsulated clumps of S protein via crosslinking of ENC. S protein was irreversibly encapsulated in endospermic nanocellulose (ENC) matrix due to crosslinking. Thin nanoparticles of 1–5 nm are seen in a crosslinked scaffold; **(b)** Fluorescent S protein encapsulated in an ENC dried gel by differential interference contrast (DIC) imaging with fluorescent (488 nm excitation) confocal microscopy: **(i)** DIC image of the ENC membrane; **(ii)** fluorescent confocal image of entrapped Alexa Fluor 488 S protein clumps and **(iii)** overlay of ENC membrane showing the fluorescent clumps of S protein.

imaged on the microscope. All cells were visualized by CellTrace™ Violet dye (blue), dead cells were visualized by propidium iodide (red) staining, and infected cells were GFP positive (green). Positive control cells (Fig. 3b) were viable (few red cells) and demonstrated obvious signs of infection (green cells); whereas cells embedded in ENC (Fig. 3c,d) were viable (few red cells) but showed no signs of infection (no green cells) ( $n = 4$ ).

**Long-term direct cell exposure to ENC had a transitory effect on cell viability and proliferation.** To confirm that cells were viable, and that lack of infection in ENC conditions was not due to massive cell death, we evaluated cell viability in the above experiments by flow cytometry using AlexaFluor350 dye, which is taken up by dead cells. This analysis revealed small but significant decreases in cell viability in ENC conditions. The percentage of viable cells in positive controls (cells + SARS-CoV-2 pv) was  $98.29 \pm 0.23\%$  ( $n = 16$ , Fig. 4a) and cells in ACE2 + SARS-CoV-2 pv, IgG + SARS-CoV-2 pv, and ENC + IgG + SARS-CoV-2 pv conditions were similar to positive controls with  $96.76 \pm 0.88\%$ ,  $98.11 \pm 0.31\%$  and  $94.08 \pm 1.49\%$  viable cells, respectively. The percentages of viable cells in ENC + SARS-CoV-2 pv and ENC + ACE2 + SARS-CoV-2 pv conditions were statistically different from positive controls with  $94.41 \pm 1.12\%$  ( $p = 0.010$ ),  $92.44 \pm 1.66\%$  ( $p = 0.006$ ) viable cells, respectively.

To further examine the effect of ENC on cells, CellTrace™ Violet dye dilution was used to assess proliferation index (PI) of cells and a pattern similar to viability data was observed. Positive control cells had a PI of  $1.92 \pm 0.14$  ( $n = 15$ , Fig. 4b) and cells in ACE2 and IgG with SARS-CoV-2 pv conditions were not significantly different with PIs of  $1.87 \pm 0.12$  and  $2.03 \pm 0.16$  respectively. PIs for cells in ENC + SARS-CoV-2 pv, ENC + ACE2 + SARS-CoV-2 pv, and ENC + IgG + SARS-CoV-2 pv conditions were lower:  $1.66 \pm 0.10\%$  ( $p = 0.008$ ),  $1.72 \pm 0.10\%$  ( $p = 0.101$ ) and  $1.57 \pm 0.09\%$  ( $p = 0.015$ ) respectively. Cell infection by SARS-CoV-2 pv did not affect PI: infected and uninfected cells had PIs of  $1.98 \pm 0.11\%$  and  $2.00 \pm 0.11\%$  ( $n = 22$ ,  $p = 0.813$ , Fig. 4c) respectively.

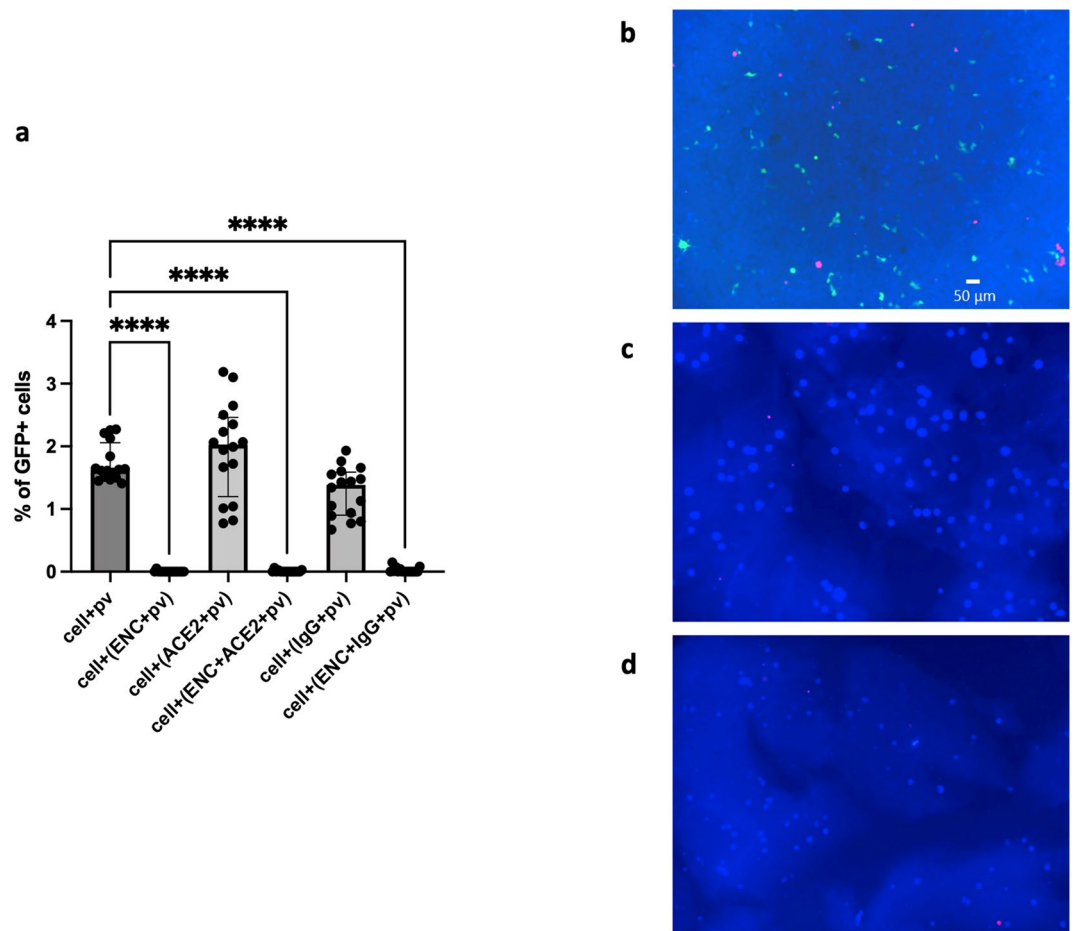


**Figure 3.** ENC prevented SARS-CoV-2 pseudovirus infection of 293T-hsACE2 cells. 293T-hsACE2 cells were inoculated with SARS-CoV-2 pseudovirus (pv) with a GFP reporter in conditions with and without endospermic nanocellulose (ENC) and molecular lures (ACE2 or anti-SARS-CoV-2 S IgG (IgG)) and incubated for 3 days. **(a)** Cells were harvested for flow cytometry analysis and % of GFP infected cells was determined for each condition ( $n = 16$ ,  $****p < 0.0001$ , Kruskal–Wallis test, median with interquartile range). Fluorescent microscopy was used to image cells embedded in ENC and challenged with pseudovirus **(b–d)**; shown is one representative experiment out of four. **(b)** infected cells in positive controls (cells + pv), **(c)** cells embedded in ENC then infected with pv or **(d)** cells embedded in ENC and infected with pv embedded in ENC. Blue represented all cells (CellTrace™ Violet), green indicated GFP infected cells, and Red indicated propidium iodide for dead cells. The ENC was visible as a faint blue cloud in **(c, d)** and demonstrates that cells are immobilized in the gel.

However, the effect of ENC on cell proliferation was transitory: experiments were performed in which cells remained in ENC conditions (indicated by (none)) as above, or were removed from all conditions after 4 h or overnight incubation (indicated by (4 h) or (O/N)), washed and returned to fresh plates without re-addition of SARS-CoV-2 pv, ENC, ACE2, and IgG. PI was evaluated 3 days post-inoculation. Results show that when ENC is removed, cells recovered and PIs of all transferred cells (indicated by (4 h) or (O/N)) were no longer significantly different in their proliferation rate from positive control cells ( $n = 3$ ,  $p = 0.264–0.999$ , Fig. 5a,b).

**ENC prevented transmission of HIV-1 into target cells.** To test whether ENC prevented infection of other viruses, we next assessed its ability to entrap HIV-1<sub>LAI.04</sub>. We infected MT-4 cells with HIV-1<sub>LAI.04</sub> in the presence of ENC. HIV-1 was diluted in NaCl and added either to culture medium or to ENC, and then applied to MT-4 cells for 4 h, washed three times in PBS, and returned to culture. HIV-1 infection was evaluated 4 days post-infection by flow cytometry measurement of p24+ cells. In control experiments without ENC, HIV-1 infected  $27.27 \pm 2.62\%$  of cells ( $n = 16$ , Fig. 6). In contrast,  $0.05 \pm 0.01\%$  of cells were infected when HIV-1 was entrapped in ENC which was significantly less than in the controls ( $p < 0.0001$ ) and not significantly above background staining of uninfected cells ( $0.04 \pm 0.01\%$  infected cells,  $p = 0.704$ ).

**The ability of ENC to completely entrap SARS-CoV-2 pv was mediated by sodium chloride.** We next examined the mechanism of ENC virus entrapment. It is known that sulfonation of nanocellulose results

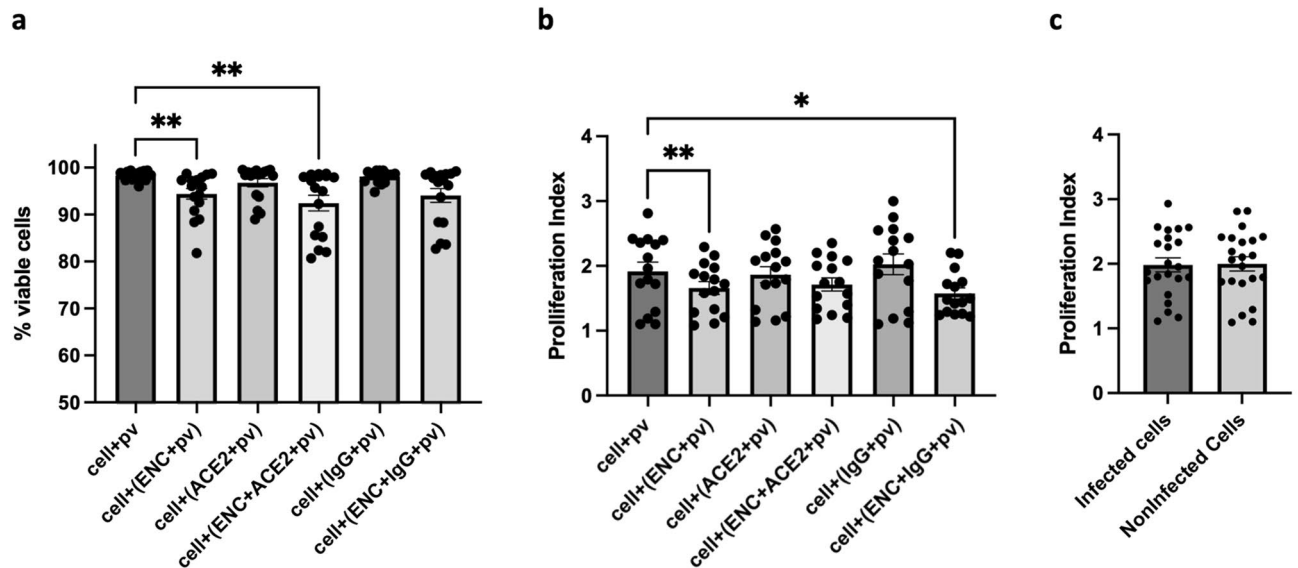


**Figure 4.** Viability and proliferation index was lower for cells in ENC. 293T-hsACE2 cells were inoculated with SARS-CoV-2 pseudovirus (pv) in conditions with and without endospermic nanocellulose (ENC) and molecular lures (ACE2 or anti-SARS-CoV-2 S IgG (IgG)) and incubated for 3 days. Cells were harvested for flow cytometry analysis. Statistical comparisons were made between positive controls (cells + pv) and other conditions. **(a)** % of viable cells was calculated for each condition ( $n = 16$ ,  $**p < 0.01$ , Kruskal–Wallis test, median with interquartile range). **(b)** Proliferation index was measured by CellTrace Violet™ dye dilution for all conditions ( $n = 15$ ,  $*p < 0.05$ ,  $**p < 0.01$ , ANOVA, mean  $\pm$  SEM) and **(c)**. Proliferation index was compared between infected and noninfected cells in positive controls (cells + pv) ( $n = 22$ ,  $p = 0.812$ , ANOVA, mean  $\pm$  SEM).

in ionic functionalization of cellulose nanoparticles that allow crosslinking mediated by positively charged ions such as sodium and calcium. We therefore tested whether this was indeed the mechanism by which virus was encapsulated within ENC. Conditions for SARS-CoV-2 pv infection were modified such that NaCl solutions were replaced with culture medium in the above experiments. In conditions without ENC, we observed infected cells similar to the above-mentioned experiments:  $2.31 \pm 0.34\%$  and  $2.74 \pm 0.43\%$  in cells + SARS-CoV-2 pv, cells + (ACE2 + SARS-CoV-2 pv), respectively; however, the condition of cells + (IgG + SARS-CoV-2 pv) did have lower infection:  $1.55 \pm 0.26\%$  infected cells, ( $p = 0.009$ ,  $n = 11$ , Fig. 7). Cells in ENC conditions showed significant reductions in SARS-CoV-2 pv infection compared to control infected cells (cells + SARS-CoV-2 pv):  $1.37 \pm 0.28\%$  ( $p = 0.007$ ),  $1.43 \pm 0.26\%$  ( $p = 0.024$ ) and  $0.79 \pm 0.17\%$  ( $p = 0.002$ ) infected cells for cells + (ENC + SARS-CoV-2 pv), cells + (ENC + ACE2 + SARS-CoV-2 pv) and cells + (ENC + IgG + SARS-CoV-2 pv) conditions respectively. However, the percentage of infected cells was higher than in the above experiments where NaCl was used for crosslinking the ENC and infection was almost completely suppressed.

## Discussion

The current study reports on a nanocellulose that is capable of efficiently preventing viral infection. Nanocellulose derived from ivory nut endosperm yields small nanoparticles (1–5 nm) which provide high surface area for entrapment of microbes. Here, we demonstrate ENC as a universal binder that prevents viral infection of cells. ENC was shown to nanoencapsulate S protein of SARS-CoV-2, as well as whole SARS-CoV-2 pv and HIV-1 virions. Moreover, ENC demonstrated the ability to immobilize IgG and ACE2 recombinant protein that were utilized with high specificity as molecular lures to bind and immobilize SARS-CoV-2 pv.

ENC suspensions, when crosslinked, form hydrogels that result from the entanglement of nanoparticles mediated by electrostatic stabilization associated with positively charged molecules such as sodium, calcium and potassium ions. This crosslinking causes sol-to-gel transitions that are irreversible. The ENC particle aggregation that occurs during sol-to-gel transitions is a phenomenon ubiquitous in colloidal and aerosol systems, including nanocellulose aqueous suspensions. Upon dispersion, particles collide and often irreversibly stick together to form larger clusters of a fractal-like morphology<sup>19</sup>. The crosslink density of the gels is dependent on the concentration of nanoparticles, while the pore size of the matrix is an inverse function of the concentration<sup>20</sup>. Different chemical routes of surface functionalization of the nanocellulose can provide ionic surfaces via phosphorylation, carboxymethylation, oxidation, and sulfonation, or promote hydrophobic interactions through acetylation, etherification, silylation, urethanization, and amidation<sup>21</sup>. Here we used sulfonated ENC which allows electrostatic interactions between the cellulose's active groups and charged moieties in proteins such as those on the surface of viruses.

The feasibility of ENC as an inhibitor of viral transmission was first verified by ELISA, which demonstrated effective blocking of SARS-CoV-2 S protein interaction with ACE2 in the presence of ENC, and allowed us to identify optimal working concentrations of ENC. AFM and confocal microscopy validated these results, showing entrapment of S protein in ENC.

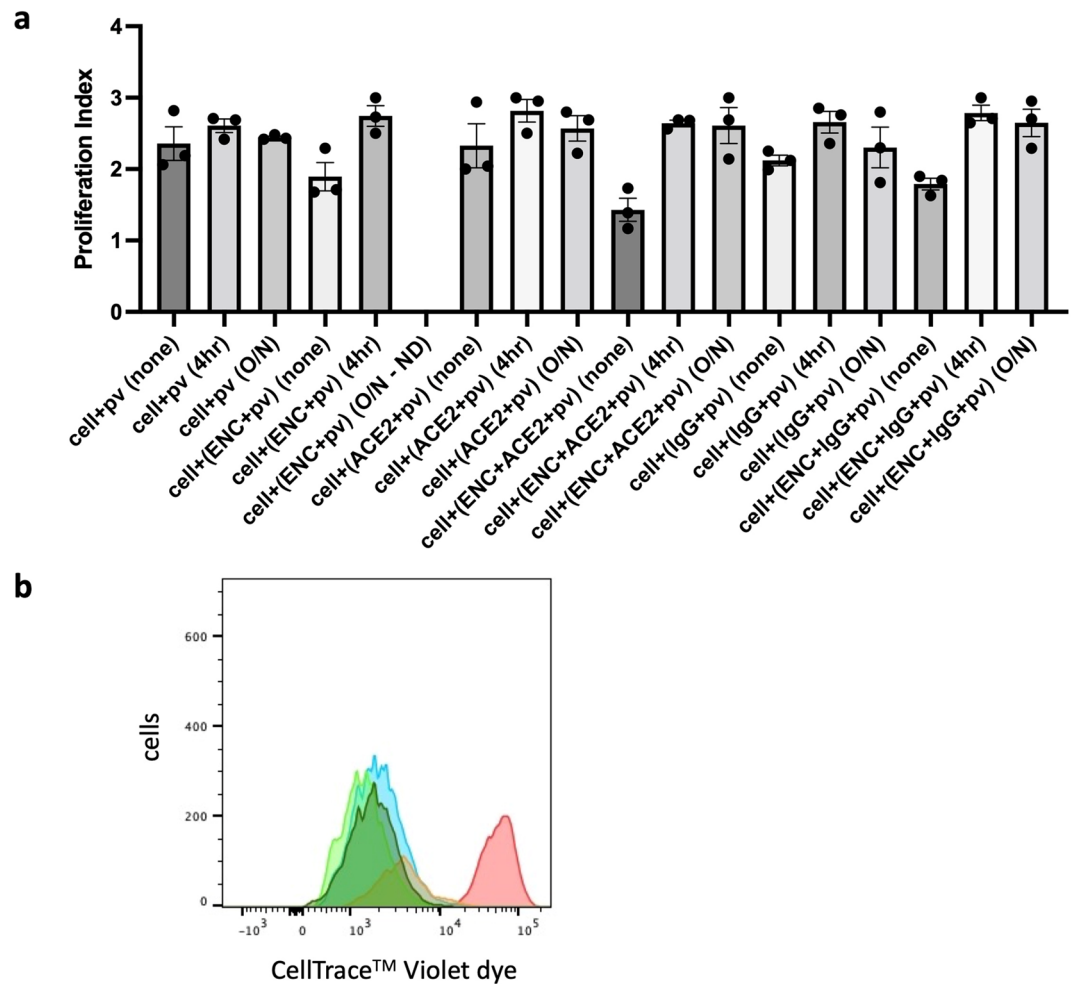


**Figure 5.** Proliferation index recovered when ENC was removed. 293T-hsACE2 cells were inoculated with SARS-CoV-2 pseudovirus (pv) in conditions with and without endospersive nanocellulose (ENC) and molecular lures (ACE2 or anti-SARS-CoV-2 S IgG (IgG)) and incubated for 3 days (none) or cells were removed from ENC conditions after 4 h (4 h) or overnight (O/N) and cultured in new plates. Cells were harvested for flow cytometry analysis and proliferation index was measured by CellTrace Violet™ dye dilution for all conditions. **(a)** Proliferation of cells in transfer conditions (denoted by (4 h) or (O/N)) was not significantly different from positive controls (cells + pv) ( $n = 3$ ,  $p = 0.264$ – $0.999$ , ANOVA, mean  $\pm$  SEM). **(b)** Histogram of CellTrace Violet™ dye dilution for initial staining intensity (red) and for cells + pv (blue), cells + (ENC + pv) no transfer (orange), cells + (ENC + pv) 4 h transfer (light green) and cells + (ENC + pv) overnight transfer (dark green). Shown is one representative experiment out of three. ND, not done.

Results from SARS-CoV-2 pv infection of 293T-hsACE2 cells demonstrated that ENC essentially eliminated infection, as no or few cells were infected. Previous studies have shown that nanocelluloses are effective membrane filters to remove viruses but they have not been employed to demonstrate prevention of viral infection<sup>22</sup>. Antiviral activity of alginate-based<sup>5</sup> or sialic acid<sup>6</sup> materials have been shown, but the modes of action and applications are different from those of ENC. Our study demonstrates the ability to block infection whether SARS-CoV-2 pv was directly entrapped in ENC, or whether molecular lures (ACE2 or anti-SARS-CoV-2 IgG) were first entrapped and then allowed to bind SARS-CoV-2 pv. Molecular lures have been used to trap both viruses in general or specific viruses<sup>23–25</sup>, but the ability to design lures in ENC described here provides an alternate biocompatible method of entrapment. ACE2 and anti-SARS-CoV-2 IgG added directly to the culture medium were not effective at preventing infection. This may be due to the fact that these experiments were performed with conditions that maximize the chance of infection; therefore, the design did not allow for optimal inhibition with ACE2 or IgG, which typically would require a short incubation time between cells and virus followed by removal of virus.

Also, infection was prevented when cells were embedded in ENC. This also points to the universal binding property of ENC, as it can entrap not only microorganisms, but also eukaryotic cells. This expands the possibilities for other applications of ENC.

Exposure of cells to ENC for three days resulted in small decreases in cell viability and of proliferation indexes. However, these effects were transient as demonstrated by cell transfer assays. If cells were removed from ENC conditions after 4 h or overnight incubation with ENC, their proliferation indexes returned to normal. Although

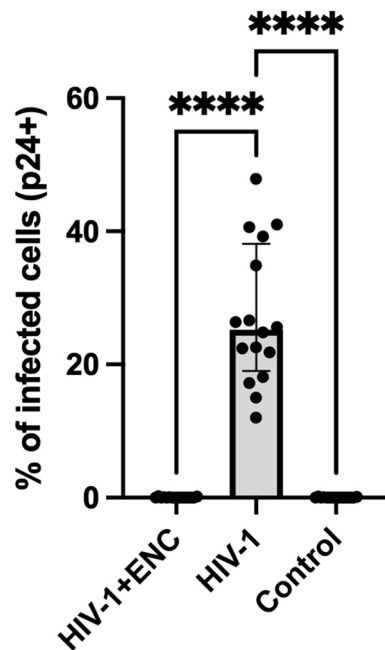


**Figure 6.** ENC prevented HIV-1 infection of MT-4 cells. MT-4 cells were inoculated with HIV-1<sub>LAI.04</sub> in conditions with and without endospemic nanocellulose (ENC) for four hours, thoroughly washed and cultured for four days. Cells were harvested for flow cytometry analysis and infection measured by intracellular p24 staining. No infection of cells was observed in cells when virus was entrapped in ENC ( $n = 16$ , \*\*\*\* $p < 0.0001$  compared to positive control cells, Kruskal–Wallis test, median with interquartile range). The level of intracellular p24 in HIV-1 + ENC conditions was not different from negative control cells with no HIV-1.

we did not address the mechanism for these decreases, we believe it may be related to insufficient gas exchange or nutrient transfer through the relatively thick ENC gels on top of the cells. In future applications of this technology, it is unlikely that cells will be directly exposed to thick layers of ENC for long periods of time. In general, nanocellulose based biomaterials have high biocompatibility and low toxicity thus they are being developed for many biomedical applications<sup>26</sup>.

The ability of ENC to prevent viral transmission was not unique to SARS-CoV-2, as experiments with infectious HIV-1 demonstrated a similar effect. HIV-1 infection was almost completely suppressed when virus was entrapped in ENC. Thus, with a second virus, we showed the ability to block infection of cells by entrapping virus in ENC. Previous studies have shown the ability of various types of nanocellulose to efficiently remove viruses using membrane filtration<sup>22</sup> but here we not only trap virus in ENC, but also demonstrate ENC biological effectiveness.

Taken altogether, these results demonstrate wide potential applicability of ENC that can bind individual proteins (S protein, ACE2, IgG), different virus particles (SARS-CoV-2 pv and HIV-1) and whole cells. The electrostatic interactions between the functionalized ENC and proteins form irreversible crosslinked hydrogels. Nanocellulose is being explored for many biomedical applications due to its ability to immobilize proteins while preserving their structural integrity and enhancing their bioactivity and stability<sup>26</sup>. To demonstrate the mechanism of entrapment by ENC, we established the importance of positively charged molecules, in this case NaCl, in crosslinking the ENC to permanently entrap particles. When NaCl was omitted from ENC preparations, some viral particles were able to escape the ENC scaffold and infect cells.

Our study does have several limitations. We assessed only a few proteins and viruses, and entrapment was assessed only over a relatively short period of time. Also, for future applications, more elaborate characterization of ENC will be required. Potential risks associated with the use of nanoparticles are a concern for bioaccumulation and other potential subcellular interactions. For instance, in *in vivo* experiments with respirable nanocellulose and cellulose dust, one month of exposure resulted in granulomatous inflammation, fibrosis, and alveolobronchiolitis<sup>27</sup>. In contrast, the ENC particles utilized in this work, due to their dense negative charge provided by  $\text{SO}_3^-$  groups from sulfuric acid synthesis, instantaneously crosslink in the presence of positive ions and molecules, changing from nanostructured materials to macrostructured scaffolds which are unable to penetrate tissues or be internalized by phagocytes. Rather, they can embed cells, viruses, and molecules. ENC particles act as building blocks that are assembled together into large crosslinked structures.

ENC is particularly well suited as a universal binder due to its high surface area for entrapment<sup>7</sup>. The ability of ENC to encapsulate viral particles thus preventing their ability to infect target cells, as well as to also entrap proteins and cells, demonstrate the usefulness of this biomaterial for development of new strategies to prevent viral transmission. This material has potential applications as a film for masks and filters, to bind viral particles and increasing the effectiveness of these filtration devices, or to create adsorbent surfaces to capture or inactivate viruses. The concentrations of ENC used in these experiments will lend themselves easily to aerosolization making



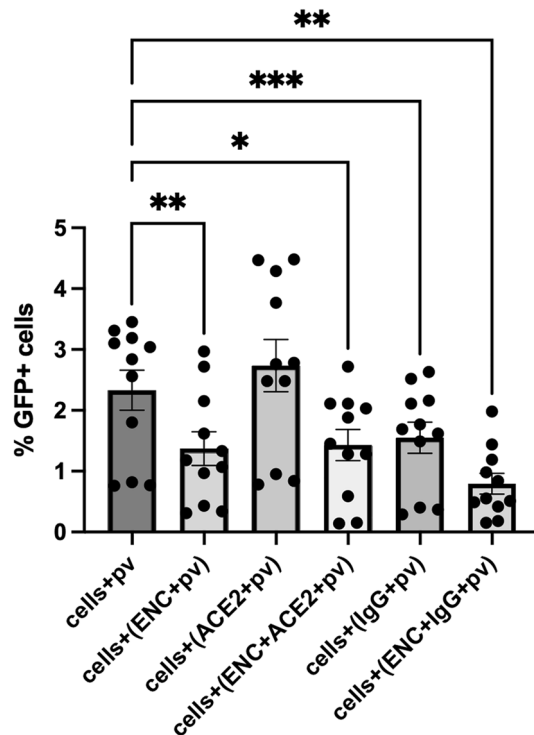


**Figure 7.** NaCl was critical for crosslinking and capture of virus in ENC. 293T-hsACE2 cells were inoculated with SARS-CoV-2 pseudovirus (pv) with a GFP reporter in conditions with and without endospermic nanocellulose (ENC) and molecular lures (ACE2 or anti-SARS-CoV-2 S IgG (IgG)) and incubated for 3 days, as in previous experiments except that NaCl was replaced with culture medium in preparation of reagents. Cells were harvested for flow cytometry analysis and % of GFP infected cells was displayed for each condition (n = 16, \* $p < 0.05$ , \*\* $p < 0.01$ , \*\*\* $p < 0.001$ , ANOVA, mean  $\pm$  SEM). ENC reduced but did not completely inhibit infection as in experiments where ENC was crosslinked by NaCl.

them ideal for such purposes. Nanoparticles that are deemed safe for in vivo use also have potential to enhance bioavailability of natural compounds, or for drug delivery.

## Materials and methods

**Nanocellulose synthesis.** ENC was synthesized from ivory nut endosperm by grinding Tagua seeds to a particle size of  $< 200 \mu\text{m}$  then subjecting the flour (20 g) to acid hydrolysis in 8 M sulfuric acid at 1:10 ratio (grams of flour: grams of sulfuric acid) at  $60^\circ\text{C}$  for 2.5 h at 300 rpm. The reaction was stopped with an equal volume of deionized water. The suspension was collected in a 50 ml tube, centrifuged at 3000 rpm for 10 min, supernatant discarded, and the pellet resuspended in deionized water and dialyzed for one week, until reaching pH 5.

**Adjustment of ENC w/v percentage.** ENC percentage w/v in the hydrogel was determined on three samples of 10 ml of hydrogel dried at  $80^\circ\text{C}$  for 48 h. The dried ENC was weighed to calculate % w/v then diluted to 0.25% w/v and stored at  $4^\circ\text{C}$ .

**Titration of  $\text{SO}_3^-$  groups.** Conductimetric titration was used to measure  $-\text{SO}_3\text{H}$  groups of ENC that result from acid hydrolysis according to previously published methods<sup>28</sup>. The sample was prepared as follows: 2.5 g of sample suspension containing 0.803% w/v ENC was suspended in water. The sample was diluted in 120 ml of 1 mM NaCl solution, and neutralized with NaOH (2 mM) added in 0.1 ml aliquots at 30 s intervals<sup>29</sup>. The sulfate group's content was determined after three subsequent measurements<sup>30</sup>. The average value of volume of NaOH and conductometry were taken in order to plot the titration curve. The ester sulfate content of the samples was calculated using the equation:  $X = C_t \cdot V_1 / m$  where:  $X$  is the sulfate group's content in  $\mu\text{mol/g}$ ;  $C_t$  is the concentration of the NaOH solution, in  $\mu\text{mol/l}$ ;  $V_1$  is the volume of the NaOH solution consumed at the first intersection point in litres, and  $m$  is the oven-dry weight of sample in grams.

**ELISA tests.** Quantitative SARS-CoV-2 Neutralizing Antibody ELISA Kit (Epitope Diagnostics, San Diego, CA) was used with modifications where S protein was preincubated with ENC before mixing with ACE2 reagent. This modification was introduced upon consultation with the manufacturer who guided us through this modified assay. Briefly, duplicate calibrator, controls, and samples were set up with 25  $\mu\text{l}$  per well with 50  $\mu\text{l}$  of HRP labeled spike protein, 40  $\mu\text{l}$  of ENC at different percentages (0.5; 0.4; 0.33; 0.27; 0.16; and 0.1) w/v, and 10  $\mu\text{l}$  of

0.015 M NaCl. 50  $\mu$ l of biotinylated ACE2 was added, mixed and incubated at room temperature for 45 min in the dark. Wells were washed 5 times, 100  $\mu$ l substrate was added, plate was incubated at room temperature for 20 min in the dark, 100  $\mu$ l of stop solution was added, and plate was read within 10 min on microplate reader at 450 nm absorbance.

**Atomic force microscopy.** 20  $\mu$ l of ENC was deposited on a clean glass slide and 5  $\mu$ l of different concentrations of SARS-CoV-2 S protein were dropped on top. The mix was left to interact then dry in ambient conditions. Atomic force microscopy (AFM) imaging was performed in air on a Bioscope Catalyst AFM (Bruker-nano, Santa Barbara, CA), in the “tapping” mode, using silicon cantilevers with nominal stiffness of 2.8 N/m and resonance frequency of 75 kHz (FESP cantilevers by Bruker-nano). Acquired images were post-processed using the instrument software (Nanoscope Analysis, v.2.0, Bruker-nano).

**Fluorescence confocal microscopy.** Images of dry membranes resulting from pre-washed and dried ENC hydrogels encapsulating fluorescent S protein were acquired with an Olympus FV3000RS laser scanning confocal microscope using Peltier-cooled GaAsP detectors. Detector emission was automatically optimized for AlexaFluor 488 using a spectral system comprised of a volume phase holographic spectral transmission grating and adjustable slit. Images were collected with 30X silicon immersion objective (UPLSAPO30XS; NA 1.05; Olympus Tokyo). Spots on the bottom of a 35 mm glass bottom dish were acquired using multi-area time-lapse (MATL). Image fields were stitched with Olympus Fluoview software (FV31S-SW, Tokyo, Japan). Pixels were sampled by the Nyquist criterion.

**Cell lines and pseudoviruses/viruses.** 293T-hsACE2 cells (Integral Molecular, Philadelphia, PA), target cells for SARS-CoV-2 pv, were cultured in DMEM, 10% FBS, 50  $\mu$ g/ml gentamicin, 2.5  $\mu$ g/ml amphotericin B and 0.5  $\mu$ g/ml puromycin. SARS-CoV-2 S protein (Wuhan-Hu-1:D614) pseudotyped lentiviral stocks (Virongy, Manassas, VA) contained green fluorescent protein (GFP) reporters and were quantified by p24 content.

MT-4 cells (ATCC, Manassas, VA), target cells for HIV-1<sub>LAI.04</sub>, were cultured in RPMI 1640, 10% FBS, 50  $\mu$ g/ml gentamicin and 2.5  $\mu$ g/ml amphotericin B. HIV<sub>LAI.04</sub> viral stock (Virology Quality Assurance Laboratory, Rush University, Chicago, IL) was quantified by p24 content.

Cell experiments were performed with 0.25% ENC, and recombinant ACE2 receptor (ACE2) and anti-SARS-CoV-2 S IgG (IgG) from Quantitative SARS-Cov-2 Neutralizing Antibody ELISA kit diluted 1:10 in 0.9 M NaCl.

**Pseudovirus entry assay.** 293T-hsACE2 cells ( $4 \times 10^4$ /well) in 100  $\mu$ l of culture medium were placed in 96-well plates. SARS-CoV-2 pv (pv) was diluted in 0.9 M NaCl for 100 ng/ml final p24 concentration. Conditions were set up in 3–4 replicates: (1) cells + pv: 10  $\mu$ l pv resuspended in 90  $\mu$ l medium; (2) cells + (ENC + pv): 10  $\mu$ l pv in 90  $\mu$ l ENC; cells + (ACE2 + pv): 10  $\mu$ l pv in 90  $\mu$ l ACE2; (3) cells + (ENC + ACE2 + pv): 80  $\mu$ l of ENC incubated with 10  $\mu$ l ACE2 for 15 min, then 10  $\mu$ l pv added; (4) cells + (anti-SARS-CoV-2 IgG + pv): 80  $\mu$ l medium, 10  $\mu$ l IgG and 10  $\mu$ l pv; (5) cells + (ENC + IgG + pv): 80  $\mu$ l ENC incubated with 10  $\mu$ l IgG for 15 min then 10  $\mu$ l pv added. Solutions were incubated for 30 min at room temperature, added to cells and incubated for three days at 37 °C, 5% CO<sub>2</sub>. Pseudoviral entry was observed by fluorescent microscopy and flow cytometry. Identical experiments were performed except that NaCl in all solutions was replaced with culture medium.

Cells to be embedded in ENC were resuspended in NaCl with 10  $\mu$ l cells at  $4 \times 10^6$  cells/ml added to 90  $\mu$ l ENC for each well, and pv was added either as free pv or ENC encapsulated pv (10  $\mu$ l pv in NaCl in 90  $\mu$ l of medium or ENC).

For transfer experiments, cells were harvested after 4 h or overnight incubation by trypsinization with 0.25% Trypsin–EDTA and centrifugation at 400xg for 5 min. Cells were washed twice with PBS, centrifuged, and cultured for the remainder of the 3 days in new plates.

**HIV infection assay.** MT-4 cells ( $5 \times 10^4$ /well) in 100  $\mu$ l of medium were placed in 96-well plates. Cells were inoculated with 1 ng/ml of HIV-1 p24 content diluted in 0.9 M NaCl. Conditions were set up in 3–4 replicate wells: cells + HIV: 10  $\mu$ l HIV-1 in 90  $\mu$ l medium; cells + (ENC + HIV): 10  $\mu$ l HIV-1 in 90  $\mu$ l ENC; and cells only: 10  $\mu$ l NaCl in 90  $\mu$ l medium. Solutions were incubated for 20 min, added to cells and cultured for 4 days.

**Fluorescence microscopy and flow cytometry.** Pseudovirus infection was monitored by visualization of GFP positive cells after three days on a fluorescent microscope (Keyence BZ-X810, Itasca, IL) equipped with filter cubes for GFP, Texas Red and DAPI. For cell embedding conditions, gels were transferred to microscope slides, stained with propidium iodide (Thermo Fisher, Waltham, MA, 1  $\mu$ g/ml in PBS), coverslipped and imaged.

Following imaging, cells were harvested by trypsinization, washed and labeled with Alexa Fluor 350 dye (ThermoFisher, 1  $\mu$ g/ml) for viability, and acquired on a Symphony A5 flow cytometer (BD Biosciences, Franklin Lakes, NJ). Flow cytometry analysis included size gating on FSC vs SSC plots, single cells on FSC-A vs FSC-H plots, live cells by viability dye exclusion with BUV450 vs SSC, and BB515 staining for percent of GFP + cells. Analysis was performed in FlowJo v10.8 (BD Biosciences).

For proliferation, cells were prelabeled with Celltrace™ Violet (ThermoFisher) by suspension in 1 ml of PBS with 1  $\mu$ l of dye, incubated for 20 min at 37 °C, and washed, with an aliquot fixed immediately. Cells were analyzed by flow cytometry with gating as above, followed by BV421 histograms for the proliferation modeling tool in FlowJo. Proliferation index (PI) was based on dye loss and was calculated as the total number of divisions divided by the number of cells that went into division.

For determining HIV infection, cells were labeled with viability dye, fixed and permeabilized (Fix and Perm™ cell permeability kit, ThermoFisher), then stained with mouse anti-p24 (KD57-RD1, Beckman Coulter, Brea, CA), washed and fixed in 2% paraformaldehyde. Cells were acquired on flow cytometer and p24+ infected cells were identified.

**P24 measurement by Luminex.** SARS-CoV-2 pseudotyped lentiviral stocks and HIV-1<sub>LAI.04</sub> were quantified using a p24 cytometric bead assay<sup>31</sup>.

**Statistical evaluation.** Data normality was tested using D'Agostino and Pearson test or Shapiro–Wilk test when *n* was small. Normal data were analyzed by one-way analysis of variance and presented as mean ± standard error of the mean (SEM). Data not normally distributed were analyzed by Kruskal–Wallis Rank test and presented as median with interquartile range. GraphPad Prism v9.2.0 (GraphPad Software, San Diego, CA) was used for statistics with *p* < 0.05 considered statistically significant.

## Data availability

All data generated or analyzed during this study are included in this published article (and its Supplementary Information files).

Received: 13 October 2022; Accepted: 17 April 2023

Published online: 28 April 2023

## References

1. Chu, D. K. *et al.* Physical distancing, face masks, and eye protection to prevent person-to-person transmission of SARS-CoV-2 and COVID-19: a systematic review and meta-analysis. *Lancet* **395**, 1973–1987. [https://doi.org/10.1016/S0140-6736\(20\)31142-9](https://doi.org/10.1016/S0140-6736(20)31142-9) (2020).
2. Dowell, D., Lindsley, W. G. & Brooks, J. T. Reducing SARS-CoV-2 in shared indoor air. *JAMA* **328**, 141–142. <https://doi.org/10.1001/jama.2022.9970> (2022).
3. Huang, X. *et al.* Antiviral biomaterials. *Matter-Us* **4**, 1892–1918. <https://doi.org/10.1016/j.matt.2021.03.016> (2021).
4. Jones, S. T. *et al.* Modified cyclodextrins as broad-spectrum antivirals. *Sci. Adv.* **6**, eaxx318. <https://doi.org/10.1126/sciadv.aax9318> (2020).
5. Serrano-Aroca, A., Ferrandis-Montesinos, M. & Wang, R. Antiviral properties of alginate-based biomaterials: Promising antiviral agents against SARS-CoV-2. *ACS Appl. Bio. Mater.* **4**, 5897–5907. <https://doi.org/10.1021/acsabm.1c00523> (2021).
6. Petitjean, S. J. L. *et al.* Multivalent 9-O-acetylated-sialic acid glycoclusters as potent inhibitors for SARS-CoV-2 infection. *Nat. Commun.* <https://doi.org/10.1038/s41467-022-30313-8> (2022).
7. Mattos, B. D. *et al.* Nanofibrillar networks enable universal assembly of superstructured particle constructs. *Sci. Adv.* **6**, eaz7328. <https://doi.org/10.1126/sciadv.aaz7328> (2020).
8. Tayeb, A. H., Amini, E., Ghasemi, S. & Tajvidi, M. Cellulose nanomaterials-binding properties and applications: A review. *Molecules* <https://doi.org/10.3390/molecules23102684> (2018).
9. Kichler, V. *et al.* A novel antimicrobial-containing nanocellulose scaffold for regenerative endodontics. *Restor. Dent. Endod.* **46**, e20–e16. <https://doi.org/10.5395/rde.2021.46.e20> (2021).
10. Li, J. *et al.* Nanocellulose-based antibacterial materials. *Adv. Healthc. Mater.* **7**, e1800334. <https://doi.org/10.1002/adhm.201800334> (2018).
11. Chen, L. & Huang, G. The antiviral activity of polysaccharides and their derivatives. *Int. J. Biol. Macromol.* **115**, 77–82. <https://doi.org/10.1016/j.ijbiomac.2018.04.056> (2018).
12. Mahira, S. J., A.; Khan, W and Domb, A. *Chapter 1. Antimicrobial Materials—an Overview.* (Royal Society of Chemistry, 2019).
13. Baghel, R. S., Reddy, C. R. K. & Singh, R. P. Seaweed-based cellulose: Applications, and future perspectives. *Carbohydr. Polym.* **267**, 118241. <https://doi.org/10.1016/j.carbpol.2021.118241> (2021).
14. Araki, J. Electrostatic or steric?—preparations and characterizations of well-dispersed systems containing rod-like nanowhiskers of crystalline polysaccharides. *Soft Matter* **9**, 4125–4141. <https://doi.org/10.1039/c3sm27514k> (2013).
15. Hubbe, M. A. *et al.* Rheology of nanocellulose-rich aqueous suspensions: A review. *BioResources* **12**, 9556–9661 (2017).
16. Gunathilake, T. M. S. U., Ching, Y. C., Uyama, H., Hai, N. D. & Chuah, C. H. Enhanced curcumin loaded nanocellulose: A possible inhalable nanotherapeutic to treat COVID-19. *Cellulose* **29**, 1821–1840. <https://doi.org/10.1007/s10570-021-04391-8> (2022).
17. Zhou, P. *et al.* A pneumonia outbreak associated with a new coronavirus of probable bat origin (vol 579, pg 270, 2020). *Nature* **588**, E6–E6. <https://doi.org/10.1038/s41586-020-2951-z> (2020).
18. Chen, B. Molecular mechanism of HIV-1 entry. *Trends Microbiol.* **27**, 878–891. <https://doi.org/10.1016/j.tim.2019.06.002> (2019).
19. Liu, P., Heinson, W. R., Sorensen, C. M. & Chakrabarty, R. K. Kinetics of sol-to-gel transition in irreversible particulate systems. *J. Colloid. Interf. Sci.* **550**, 57–63. <https://doi.org/10.1016/j.jcis.2019.04.067> (2019).
20. Curvello, R., Raghuvanshi, V. S. & Garnier, G. Engineering nanocellulose hydrogels for biomedical applications. *Adv. Colloid Interfac.* **267**, 47–61. <https://doi.org/10.1016/j.cis.2019.03.002> (2019).
21. Thakur, V., Guleria, A., Kumar, S., Sharma, S. & Singh, K. Recent advances in nanocellulose processing, functionalization and applications: A review. *Mater. Adv.* **2**, 1872–1895. <https://doi.org/10.1039/d1ma00049g> (2021).
22. Norrrahim, M. N. F. *et al.* Emerging developments regarding nanocellulose-based membrane filtration material against microbes. *Polym. (Basel)* <https://doi.org/10.3390/polym13193249> (2021).
23. Metsky, H. C. *et al.* Capturing sequence diversity in metagenomes with comprehensive and scalable probe design. *Nat. Biotechnol.* **37**, 160–168. <https://doi.org/10.1038/s41587-018-0006-x> (2019).
24. Satta, S. *et al.* An engineered nano-liposome-human ACE2 decoy neutralizes SARS-CoV-2 Spike protein-induced inflammation in both murine and human macrophages. *Theranostics* **12**, 2639–2657. <https://doi.org/10.7150/thno.66831> (2022).
25. Chen, M. *et al.* Nanotraps for the containment and clearance of SARS-CoV-2. *Matter-Us* **4**, 2059–2082. <https://doi.org/10.1016/j.matt.2021.04.005> (2021).
26. Lin, N. & Dufresne, A. Nanocellulose in biomedicine: Current status and future prospect. *Eur. Polym. J.* **59**, 302–325. <https://doi.org/10.1016/j.eurpolymj.2014.07.025> (2014).
27. Endes, C. *et al.* A critical review of the current knowledge regarding the biological impact of nanocellulose. *J. Nanobiotechnol.* <https://doi.org/10.1186/s12951-016-0230-9> (2016).
28. Azzam, F. *Assemblages thermostimulables de nanocristaux de cellulose décorés de chaînes de polymère* NNT: 2012GRENV052 thesis, (2012).

29. Dorris, A. & Gray, D. G. Gelation of cellulose nanocrystal suspensions in glycerol. *Cellulose* **19**, 687–694. <https://doi.org/10.1007/s10570-012-9679-3> (2012).
30. Johnston, L. J. *et al.* Determination of sulfur and sulfate half-ester content in cellulose nanocrystals: An interlaboratory comparison. *Metrologia* **55**, 872–882. <https://doi.org/10.1088/1681-7575/aab60> (2018).
31. Biancotto, A. *et al.* A highly sensitive and dynamic immunofluorescent cytometric bead assay for the detection of HIV-1 p24. *J. Virol. Methods* **157**, 98–101. <https://doi.org/10.1016/j.jviromet.2008.11.013> (2009).

### Acknowledgements

This work was supported by NIH intramural grant numbers: ZIA HD000713 to RDE, ZIA EB000085 to EKD, and ZIA HD008968-05 to LM; and the NIH Intramural Targeted Anti-COVID (ITAC) funding program.

### Author contributions

E.J.C-B conceived the project, R.D.F. and L.M. directed the research; E.J.C-B, W.F., and E.D. contributed to the acquisition of data, analysis; all authors analyzed data and contributed to writing the manuscript; and all authors reviewed the manuscript.

### Funding

Open Access funding provided by the National Institutes of Health (NIH).

### Competing interests

The authors declare no competing interests.

### Additional information

**Supplementary Information** The online version contains supplementary material available at <https://doi.org/10.1038/s41598-023-33686-y>.

**Correspondence** and requests for materials should be addressed to R.D.F.

**Reprints and permissions information** is available at [www.nature.com/reprints](http://www.nature.com/reprints).

**Publisher's note** Springer Nature remains neutral with regard to jurisdictional claims in published maps and institutional affiliations.



**Open Access** This article is licensed under a Creative Commons Attribution 4.0 International License, which permits use, sharing, adaptation, distribution and reproduction in any medium or format, as long as you give appropriate credit to the original author(s) and the source, provide a link to the Creative Commons licence, and indicate if changes were made. The images or other third party material in this article are included in the article's Creative Commons licence, unless indicated otherwise in a credit line to the material. If material is not included in the article's Creative Commons licence and your intended use is not permitted by statutory regulation or exceeds the permitted use, you will need to obtain permission directly from the copyright holder. To view a copy of this licence, visit <http://creativecommons.org/licenses/by/4.0/>.

This is a U.S. Government work and not under copyright protection in the US; foreign copyright protection may apply 2023